Please cite this article as: D.Yang and A.S.Morgans, A semi-analytical model for the acoustic impedance of finite length circular holes with mean flow, Journal of Sound and Vibration, xx (xxxx). http://dx.doi.org/10.1016/j.jsv.2016.08.006

A semi-analytical model for the acoustic impedance of finite length circular holes with mean flow

Dong Yang*, Aimee S. Morgans

Department of Aeronautics, Imperial College London, London, UK

Abstract

The acoustic response of a circular hole with mean flow passing through it is highly relevant to Helmholtz resonators, fuel injectors, perforated plates, screens, liners and many other engineering applications. A widely used analytical model [M. S. Howe. On the theory of unsteady high Reynolds number flow through a circular aperture, Proc. of the Royal Soc. A. 366, 1725 (1979), 205223] which assumes an infinitesimally short hole was recently shown to be insufficient for predicting the impedance of holes with a finite length. In the present work, an analytical model based on the Green's function method is developed to take the hole length into consideration for "short" holes. The importance of capturing the modified vortex noise accurately is shown. The vortices shed at the hole inlet edge are convected to the hole outlet and further downstream to form a vortex sheet. This couples with the acoustic waves and this coupling has the potential to generate as well as absorb acoustic energy in the low frequency region. The impedance predicted by this model shows the importance of capturing the path of the shed vortex. When the vortex path is captured accurately, the impedance predictions agree well with previous experimental and CFD results, for example predicting the potential for generation of acoustic energy at higher frequencies. For "long" holes, a simplified model which combines Howe's model with plane acoustic waves within the hole is developed. It is shown that the most important effect in this case is the acoustic non-compactness of the hole.

1. Introduction

A model to predict the acoustic response of a circular hole is relevant to many engineering applications. Many practical situations involve a mean flow passing through such holes, such as the cooling flow passing through perforated liners or Helmholtz resonators in aero-engine or land-based gas turbine combustors [1–4], and the fuel-air mixture passing through the injector into a combustor [5, 6]. At high Reynolds numbers, viscous dissipation is small except in the vicinity of the hole edge where the action of viscosity is mainly limited to bringing about the generation of vortices [7]. At low frequencies, significant acoustic attenuation occurs due to the conversion of acoustic energy into the sound induced unsteady shedding of vortices from the lip of the hole.

An analytical model for the acoustic response of an infinitesimally short circular hole was derived by Howe [8]. This assumed the input acoustic wavelength to be much larger than the hole dimensions, with vortices shed from the hole lip then convecting with the hole inlet mean velocity to form a thin, semi-infinitely long cylindrical vortex sheet with the same radius as the hole. The vortex strength is determined by a Kutta condition, requiring that the fluctuation velocity and pressure remain finite at the hole inlet edge. The Rayleigh conductivity, $K_R = \mathrm{i}\omega\rho\widetilde{Q}/\Delta\widetilde{p}$, denotes the relation between the oscillating volume flux ($\widetilde{Q}$) through the hole and the oscillating pressure difference ($\Delta\widetilde{p}$) across

*Corresponding author

Email addresses: d.yang13@imperial.ac.uk (Dong Yang), a.morgans@imperial.ac.uk (Aimee S. Morgans)

it. This was shown to be given by $K_R = 2R_h(\Gamma_R - \mathrm{i}\Delta_R)$, where R_h is the hole radius, Γ_R represents the inertia of the hole flow and is called the hole reactance and Δ_R, termed the resistance, is responsible for the absorption of acoustic energy. Both Γ_R and Δ_R are functions of the Strouhal number $S_t = \omega R_h/U_c$ where U_c is the vortex convection velocity. Howe's model can be slightly modified by adding a small mass inertial term to account for a small hole length; this approach has been widely used to predict the acoustic response of very short holes over recent years [1, 2, 9–13].

An alternative approach for predicting the acoustic impedance of a very short hole was developed by Bellucci et al. [3] based on the momentum balance of one-dimensional incompressible flow across the hole. Their model does not need to explicitly consider the shed vorticity. The resistance of the hole is mainly associated with the pressure loss caused by the flow contraction after the hole inlet, with the reactance mainly associated with the acoustic scattering either side of the hole. Prediction of the resistance relies on experimentally determining an accurate discharge coefficient and prediction of the reactance on the addition of a length correction term either side of the hole for the modified acoustic scattering.

When the hole length is of the same order as the hole diameter but not long enough to allow the separated mean flow to reattach the hole inner wall, it has been found experimentally (e.g. Jing and Sun [14], Su et al. [15]) that the hole impedance is quite different from that predicted by either Howe's or Bellucci's model. Specifically, the resistance is seen to decrease dramatically with increasing Strouhal number and may even turn negative in a specific Strouhal number region, implying that the hole is generating rather than absorbing acoustic energy. Both Howe's and Bellucci's models predict positive resistance and hence absorption of acoustic energy over the whole Strouhal number range. To deal with this problem, Jing and Sun [14] developed a numerical model using the boundary element method. In their model, the hole length was considered and the geometrical shape of the actual vortex sheet was obtained carefully from interpolation of previous experimental data [16]. The length of the vortex sheet was truncated at 100 times the hole radius. Their model provided good prediction of their experiment measurements. Recently, Su et al. [15] performed both experiments and CFD for holes of three different lengths. They compared both Howe's and Bellucci's model to show that either of these models was able to predict the finite length hole impedance, with only the CFD method which takes the hole length and the full vortex sheet shape into consideration giving the right prediction.

The resistance decrease, especially to negative values, is related to the coupling between the vortex shedding at the hole inlet edge and the sound radiated from the hole outlet expansion. The vortices shed from the hole inlet are convected along the vortex sheet to the hole outlet where they affect the sound radiation. The fed back acoustic waves, together with the oscillations generated directly by the vortex sheet, modulate the vortex generation at the inlet edge. Self-sustained oscillations related to this feedback are well known historically [17, 18], and have recently been experimentally and numerical studied by several groups [19, 20]. However, analytical models to predict the hole impedance are still needed – computational methods are too expensive and time-consuming for embedding in prediction tools, such as thermoacoustic network models [21] and for quickly obtaining design insights. Thus, the main aim of this article is to develop an analytical model which has the ability to predict the impedance of finite length holes over a large frequency range, as achieved by numerical methods [14, 15]. A theoretical model based on the Green's function method is developed in section 2. To calculate oscillations induced by the vortex sheet, the experimentally measured [16] vortex sheet shape used by Jing and Sun [14] is used. The vortex shedding strength is determined by applying the Kutta condition at the hole inlet edge. Model validation, results and discussions on the impact of hole length and vortex sheet shape on the acoustic impedance are given in section 3.

In the case of a long hole, for example when the hole length to diameter ratio is 5 – 10, as studied by Su et al. [15], the reattachment of the mean flow inside the hole needs to be considered. Again, no analytical models dealing with the acoustic response in the presence of this reattachment exist according to our knowledge. This may due to the difficulties in predicting both the vorticity generation at the sharp edge and its development downstream. In section 4 of this article, we present a simplified model based on Howe's [8] model for this case. Plane acoustic waves inside the hole are incorporated, enabling the model to predict the nonlinearly increasing resistance and reactance with frequency, which cannot be predicted by Howe's model, even when a compact mass inertial correction for the hole length is applied.

2. Theoretical model

A cylindrical hole connecting two large semi-infinitely long cylinders is shown in Fig. 1, where R denotes radius, L denotes length and M denotes Mach number. The subscript $[\,]_h$ denotes the hole, $[\,]_u$ upstream and $[\,]_d$ downstream

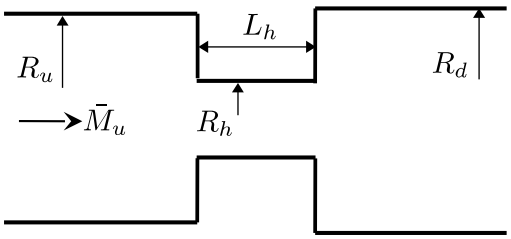

Figure 1: A hole with finite length

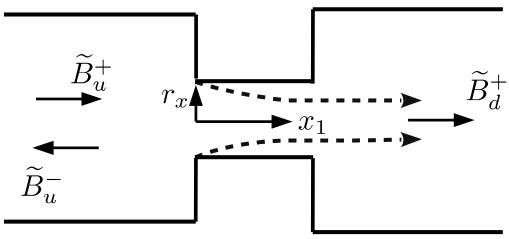

Figure 2: Acoustic waves and the shed vortex sheet

of the hole. An over bar [¯] denotes mean flow parameters. $R_u/R_h = \lambda_u$ and $R_d/R_h = \lambda_d$ are the expansion ratios upstream and downstream respectively. Mean flow Mach numbers inside the hole and far downstream of the hole outlet can be approximately calculated via $\bar{M}_h = \bar{M}_u\lambda_u^2$ and $\bar{M}_d = \bar{M}_u\lambda_u^2/\lambda_d^2$. In the low frequency region of interest, it will be shown later that an equivalent semi-infinite half-space upstream and downstream can be achieved by choosing large expansion ratios.

As shown in Fig. 2, when there is a low-frequency harmonic sound wave incident from upstream, oscillating vortices with matching frequency are shed from the hole inlet edge and are convected away along the mean streamline to form a vortex sheet. Reflected and transmitted acoustic waves are generated simultaneously. Generally the incident acoustic wavelength is much longer than the hole radius and thus the input wave can be treated as a plane wave. However, plane acoustic waves will be scattered at the hole inlet and outlet interfaces to generate high-order-mode waves (based on the hole radius), which may not be able to propagate far-away but will affect the generation of vortices near the inlet edge. At the same time, the vortex sheet also induces oscillations at the hole inlet and this will also affect the generation of vortices. A model to deal with this problem needs to consider both high-order acoustic oscillations and feedback from the vortex sheet. This is done in the following by introducing a Green's function with proper boundary conditions.

Neglecting viscosity, volume forces and entropy, the momentum equation can be written in *Crocco*'s form as [22]

$$\frac{\partial \boldsymbol{u}}{\partial t} + \nabla B = -(\boldsymbol{\omega} \times \boldsymbol{u}), \tag{1}$$

where $B = C_pT + |\boldsymbol{u}|^2/2$ denotes the stagnation enthalpy (C_p is the heat capacity at constant pressure), $\boldsymbol{u}$ the velocity and $\boldsymbol{\omega} = \nabla \times \boldsymbol{u}$ the vorticity. Mass conservation gives

$$\frac{\partial \rho}{\partial t} + \boldsymbol{u} \cdot \nabla\rho + \rho\nabla \cdot \boldsymbol{u} = 0, \tag{2}$$

where ρ denotes density.

Writing all parameters as the sum of mean and oscillating parts (e.g. $B = \bar{B} + B'$), subtracting the mean parts from both sides, combining the two equations and ignoring second-order small quantities then gives

$$\left(\frac{1}{\bar{c}^2}\left(\frac{\partial}{\partial t} + \bar{u}\frac{\partial}{\partial x_1}\right)^2 - \nabla^2\right)B' = \nabla \cdot (\boldsymbol{\omega}' \times \boldsymbol{u_c}), \tag{3}$$

where the mean velocity is assumed to be purely in the x_1 (axial) direction with value $\bar{u}$, and $\boldsymbol{u_c}$ is the vortex convection velocity which is generally assumed to be equal to mean velocity in the hole [1, 2, 14]. Equation (3) assumes that the flow is homentropic with constant mean density and sound speed ($\bar{\rho}, \bar{c}$), and with mean velocity ($\bar{u}$) much smaller than the sound speed. Strictly, $(\boldsymbol{\omega} \times \boldsymbol{u})' = \boldsymbol{\omega}' \times \bar{\boldsymbol{u}} + \bar{\boldsymbol{\omega}} \times \boldsymbol{u}'$, but the second term on the right side is ignored as it is small in comparison with the first [8, 23].

2.1. Calculating the Green's functions with proper boundary conditions

Equation. (3) is solved by introducing a Green's function $G(\boldsymbol{x}, t\,|\boldsymbol{y}, \tau)$ which satisfies

$$\left(\frac{1}{\bar{c}^2}\left(\frac{\partial}{\partial t} + \bar{u}\frac{\partial}{\partial x_1}\right)^2 - \nabla^2\right)G = \delta(\boldsymbol{x} - \boldsymbol{y})\delta(t - \tau), \tag{4}$$

where δ is the Dirac delta function, $\boldsymbol{x}$ denotes the coordinates of the space in which we want to solve the wave equation and $\boldsymbol{y}$ denotes the acoustic source location in this space. We define the specific space using a Heaviside function $H(g)$, where $g(\boldsymbol{x})$ is positive inside the space and negative outside; H equals 1 inside and 0 outside the space. Equation (3) is then rearranged to give

$$\left(\frac{1}{\bar{c}^2}\left(\frac{\partial}{\partial t}+\bar{u}\frac{\partial}{\partial x_1}\right)^2-\nabla^2\right)(B'H)=\frac{2\bar{u}}{\bar{c}^2}\frac{\partial B'}{\partial t}\frac{\partial H}{\partial x_1}-2\nabla B'\cdot\nabla H-B'\nabla^2 H+\nabla\cdot(H\boldsymbol{\omega}'\times\boldsymbol{u_c})-\nabla H\cdot(\boldsymbol{\omega}'\times\boldsymbol{u_c}), \tag{5}$$

where second-order terms in mean Mach number ($\sim \bar{u}^2/\bar{c}^2$) are ignored.

All the terms on the right side of Eq. (5) contribute as sources to B' inside the space region defined by H. Combining Eqs. (4) and (5), we obtain the expression for oscillations inside the chosen space [24]:

$$B'(\boldsymbol{x},t)H=\int_{-\infty}^{+\infty}\int_S\left[\frac{\partial G}{\partial\tau}\left(\frac{2\bar{u}}{\bar{c}^2}B'\mathbf{i}+\boldsymbol{u}'\right)-B'\nabla G\right]\cdot\mathrm{d}\boldsymbol{s}\mathrm{d}\tau-\int_{-\infty}^{+\infty}\int_V(\boldsymbol{\omega}'\times\boldsymbol{u_c})\cdot\nabla G\mathrm{d}v\mathrm{d}\tau, \tag{6}$$

where V is the space volume, S denotes the surface bounding the volume, $\mathbf{i}$ is a unit vector in the y_1 direction, $\mathrm{d}\boldsymbol{s}$ is the area vector in the normal outwards direction of the volume surface. The first integral term in Eq. (6) considers the surface acoustic source contributions and the second integral term denotes the volume acoustic source contributions of the chosen space.

A Green's function which satisfies Eq. (4) can be obtained by incorporating physical boundary conditions. As circumferential variations are neglected, the assumed system is two-dimensional. Following the method used in [23], we firstly separate the whole space region into three parts: (1) upstream region of the hole inlet where $x_1<0,\ r_x<R_u$, (2) the hole where $0<x_1<L_h,\ r_x<R_h$ and (3) downstream region of the hole outlet where $x_1>L_h, r_x<R_d$.

Boundary conditions for the upstream region (denoted by subscript $[\ ]_u$) are: (1) $\partial G_u/\partial r_x=0$ on $r_x=R_u$, which means the radial velocity on the cylinder inner surface is zero, which is equivalent to requiring the first integration in Eq. (6) over the cylinder inner surface is zero; (2) $\partial G_u/\partial x_1=0$ on $x_1=0^-$ (0^- denotes the left side of the $x_1=0$ surface, 0^+ and $L_h^\pm$ in the following are defined similarly), which means the axial velocity at this end is zero, equivalent to requiring $2\bar{u}/\bar{c}^2\partial G/\partial\tau-\partial G/\partial y_1=0$ on $y_1=0^-, r_y<R_u$ (thus the surface integration relating to these two terms in Eq. (6) is zero on $y_1=0^-, r_y<R_u$); (3) only outward waves propagate at $x_1=-\infty,\ r_x<R_u$, meaning sources inside the region only generate outward propagating oscillations, equivalent to requiring (at the $y_1=-\infty,\ r_y<R_u$ surface) that only inward waves contribute to oscillations inside the chosen space. It is worth noting that only the incident wave from the far upstream ($y_1=-\infty,\ r_y<R_u$) and the velocity oscillation at the hole inlet surface ($y_1=0, r_y<R_h$) contribute as acoustic sources to oscillations in the upstream region, and these can be calculated using Eq. (6).

In the downstream region (denoted by subscript $[\ ]_d$), similar boundary conditions are used. They are: (1) $\partial G_d/\partial r_x=0$ on $r_x=R_d$; (2) $\partial G_d/\partial x_1=0$ on $x_1=L_h^+$; (3) only outward waves propagate at $x_1=+\infty$. The procedure to calculate the Green's function is similar to that for the upstream. In this region, as well as the inlet wave from the far downstream (here assumed to be zero) and the velocity oscillation at hole outlet surface ($y_1=L_h, r_y<R_h$), the vortex sheet inside also contributes to the oscillations.

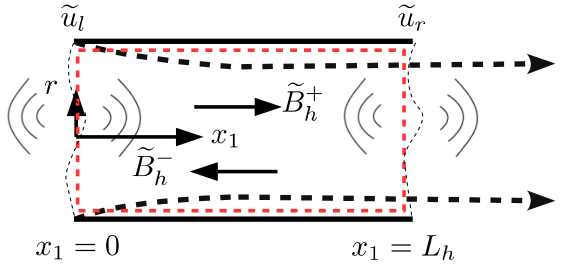

Figure 3: Waves and vortex sheet inside the hole

To calculate oscillations inside the hole (denoted by subscript $[\ ]_h$), shown as the red dashed rectangular line in Fig. 3, two Green's functions, G_h^l and G_h^r, are defined. The boundary conditions for G_h^l are: (1) $\partial G_h^l/\partial r_x=0$ on $r_x=R_h$; (2) $\partial G_h^l/\partial x_1=0$ on $x_1=0^+$; (3) only outward waves propagate at the right boundary $x_1=L_h^-$. The boundary

conditions for G_h^r are: (1) $\partial G_h^r/\partial r_x = 0$ on $r_x = R_h$; (2) $\partial G_h^r/\partial x_1 = 0$ on $x_1 = L_h^-$; (3) only outward waves propagate at the left boundary $x_1 = 0^+$. It should be noted that these two Green's functions are both defined in the whole hole region. In fact just one Green's function would be enough to solve the inhomogeneous wave equation in this region. The reason for using two is that it simplifies the expressions for oscillations on the left and right hole boundaries ($x_1 = 0^+$ and $x_1 = L_h^-$) which will be shown later to be helpful in solving the problem.

For simplicity, calculations are performed in the frequency domain with all oscillating terms assumed to have a uniform sinusoidal factor, $\exp(-\mathrm{i}\omega t)$ ($\exp(-\mathrm{i}\omega(t-\tau))$ for the Green's functions and $\exp(-\mathrm{i}\omega\tau)$ for the source terms). Thus, $G(\boldsymbol{x}, t\,|\boldsymbol{y}, \tau)$ is written in its frequency domain form $\widetilde{G}(\boldsymbol{x}, \boldsymbol{y}, \omega)$ with derivation details provided in Appendix A. These Green's functions are

$$\widetilde{G}_u = \sum_{n=0}^{+\infty} \frac{\mathrm{i}J_0(j_n r_x/R_u)J_0(j_n r_y/R_u)}{2\pi R_u^2 \gamma_u^{(n)} J_0^2(j_n)} \left[e^{\mathrm{i}\gamma_u^{(n)}|x_1-y_1|} - \frac{k_u^{n+}}{k_u^{n-}} e^{-\mathrm{i}\gamma_u^{(n)}(x_1+y_1)} \right] e^{\mathrm{i}k\bar{M}_u(y_1-x_1)}, \tag{7}$$

$$\widetilde{G}_d = \sum_{n=0}^{+\infty} \frac{\mathrm{i}J_0(j_n r_x/R_d)J_0(j_n r_y/R_d)}{2\pi R_d^2 \gamma_d^{(n)} J_0^2(j_n)} \left[e^{\mathrm{i}\gamma_d^{(n)}|x_1-y_1|} - \frac{k_d^{n-}}{k_d^{n+}} e^{\mathrm{i}\gamma_d^{(n)}(x_1+y_1-2L_h)} \right] e^{\mathrm{i}k\bar{M}_d(y_1-x_1)}, \tag{8}$$

$$\widetilde{G}_h^l = \sum_{n=0}^{+\infty} \frac{\mathrm{i}J_0(j_n r_x/R_h)J_0(j_n r_y/R_h)}{2\pi R_h^2 \gamma_h^{(n)} J_0^2(j_n)} \left[e^{\mathrm{i}\gamma_h^{(n)}|x_1-y_1|} - \frac{k_h^{n-}}{k_h^{n+}} e^{\mathrm{i}\gamma_h^{(n)}(x_1+y_1)} \right] e^{\mathrm{i}k\bar{M}_h(y_1-x_1)}, \tag{9}$$

$$\widetilde{G}_h^r = \sum_{n=0}^{+\infty} \frac{\mathrm{i}J_0(j_n r_x/R_h)J_0(j_n r_y/R_h)}{2\pi R_h^2 \gamma_h^{(n)} J_0^2(j_n)} \left[e^{\mathrm{i}\gamma_h^{(n)}|x_1-y_1|} - \frac{k_h^{n+}}{k_h^{n-}} e^{-\mathrm{i}\gamma_h^{(n)}(x_1+y_1-2L_h)} \right] e^{\mathrm{i}k\bar{M}_h(y_1-x_1)}, \tag{10}$$

where J_0 is the Bessel function of order 0 and j_n denotes the nth zero of J_1 ($J_1(j_n) = 0$ for $n = 0, 1, 2, ...$), $k = \omega/\bar{c}$, $\gamma_u^{(n)} = \sqrt{k^2 - j_n^2/R_u^2}$, $\gamma_d^{(n)} = \sqrt{k^2 - j_n^2/R_d^2}$, $\gamma_h^{(n)} = \sqrt{k^2 - j_n^2/R_h^2}$. The imaginary parts of $\gamma_u^{(n)}, \gamma_d^{(n)}, \gamma_h^{(n)}$ are taken as being positive if they are complex. The down- and upstream propagating wave numbers for the upstream region are $k_u^{n+} = -k\bar{M}_u + \gamma_u^{(n)}$ and $k_u^{n-} = -k\bar{M}_u - \gamma_u^{(n)}$ respectively (second-order terms $\sim \bar{M}_u^2$ are ignored). $k_h^{n\pm}$ and $k_d^{n\pm}$ are similarly defined for the hole and downstream regions.

2.2. Calculating the oscillations in different regions

In the frequency domain, Eq. (6) becomes

$$\widetilde{B}(\boldsymbol{x}, \omega)H = \int_S \left(2\mathrm{i}k\bar{M}\widetilde{G}\widetilde{B}\,\mathbf{i} + \widetilde{G}\nabla\widetilde{B} - \widetilde{B}\nabla\widetilde{G} \right) \cdot \mathrm{d}\boldsymbol{s} - \int_V (\widetilde{\boldsymbol{\omega}} \times \boldsymbol{u}_c) \cdot \nabla\widetilde{G}\mathrm{d}v, \tag{11}$$

using the irrotational flow relation $\mathrm{i}\omega\widetilde{G}\widetilde{\boldsymbol{u}} = \widetilde{G}\nabla\widetilde{B}$. By substituting the Green's functions in Eqs. (7, 8, 9, 10) into Eq. (11) and taking all acoustic sources into consideration within the different regions, oscillations in these regions can be obtained.

2.2.1. Oscillations upstream of the hole

Upstream of the hole inlet, since there is no vortex sheet, substituting the upstream Green's function Eq. (7) into Eq. (11) gives

$$\widetilde{B}_u(x_1, r_x) = \int_{S_{(y_1=-\infty)}} \left(2\mathrm{i}k\bar{M}_u\widetilde{G}_u\widetilde{B}\,\mathbf{i} + \widetilde{G}_u\frac{\partial\widetilde{B}}{\partial y_1}\,\mathbf{i} - \widetilde{B}\nabla\widetilde{G}_u \right) \cdot \mathrm{d}\boldsymbol{s} + \int_{S_{(y_1=0^-)}} \mathrm{i}\omega\widetilde{G}_u\widetilde{u}_l\,\mathbf{i} \cdot \mathrm{d}\boldsymbol{s} \tag{12}$$

It can be seen that any output (or upstream propagating) wave far upstream does not contribute to the first integral term as the surface integration result is zero if $\widetilde{B} \sim e^{\mathrm{i}k_u^{n-}y_1}$. The incident plane wave from far upstream is denoted by $\widetilde{B}_{u0}^+ e^{\mathrm{i}k_u^{0+}y_1}$ where $\widetilde{B}_{u0}^+$ is its amplitude and k_u^{0+} its downstream-propagating wavenumber. Substituting this into Eq. (12) and integrating over the far upstream boundary surface gives the input wave induced oscillations as

$$\widetilde{B}_u^{(1)} = \widetilde{B}_{u0}^+ \left(e^{\mathrm{i}k_u^{0+}x_1} + \frac{1-\bar{M}_u}{1+\bar{M}_u} e^{\mathrm{i}k_u^{0-}x_1} \right). \tag{13}$$

The velocity oscillation at the hole inlet surface is unknown and can be expanded as a sum of a series of Bessel functions

$$\widetilde{u}_l = \sum_{m=0}^{+\infty} U_{lm} J_0(j_m r_y / R_h). \tag{14}$$

Substituting this and the upstream Green's function into Eq. (12), and integrating over the hole inlet surface gives the hole inlet velocity induced oscillation at the upstream as

$$\widetilde{B}_u^{(2)} = 2\omega \sum_{m=0}^{+\infty} U_{lm} e^{\mathrm{i}k_u^{m-}x_1} \sum_{n=0}^{+\infty} \frac{\int_0^1 J_0(j_n r_y^*/\lambda_u) J_0(j_m r_y^*) r_y^* \mathrm{d}r_y^*}{k_u^{n-} \lambda_u^2 J_0^2(j_n)} J_0(j_n r_x / R_u), \tag{15}$$

where $r_y^* = r_y/R_h$ is the non-dimensional radical coordinate. The overall stagnation enthalpy oscillation is the sum of contributions from the input wave and the hole inlet velocity.

$$\widetilde{B}_u(x_1, r_x) = \widetilde{B}_u^{(1)} + \widetilde{B}_u^{(2)}. \tag{16}$$

For low frequencies, $k_u^{m-} = -k\bar{M}_u - \gamma_u^{(m)}$ is complex when $m > 1$ which means only the plane wave ($m = 0$) propagates to the far upstream and thus the overall stagnation enthalpy oscillation far upstream can be written as

$$\widetilde{B}_u(x_1 \to -\infty) = \widetilde{B}_{u0}^{+} e^{\mathrm{i}k_u^{0+}x_1} + \left(\frac{1-\bar{M}_u}{1+\bar{M}_u} \widetilde{B}_{u0}^{+} - \frac{U_{l0}\bar{c}}{(1+\bar{M}_u)\lambda_u^2} \right) e^{\mathrm{i}k_u^{0-}x_1}. \tag{17}$$

Equation (17) is important as it shows that the low frequency acoustic response far upstream of a hole is a function of the zeroth-order velocity oscillation at the hole inlet surface. However, higher-order contributions to $\widetilde{u}_l$ still need to be calculated in order to calculate U_{l0}. This can be achieved using the condition that the stagnation enthalpy oscillation is continuous across the hole inlet surface [8, 14, 23]. Oscillations induced by the shed vortex sheet which is convected downstream of the hole inlet edge need to be considered. The hole length is accounted for by considering the hole region separately and applying stagnation enthalpy continuity again across the hole outlet surface. The vortex sheet strength is calculated using the Kutta condition, requiring the velocity $\widetilde{u}_l$ to be zero at the hole inlet edge ($y_1 = 0,\ r_y = R_h$). This is equivalent to requiring that the axial derivation of the stagnation enthalpy is zero.

2.2.2. Oscillations inside the hole

Inside the hole, shown in Fig. 3, the stagnation enthalpy oscillations are calculated by substituting $\widetilde{G}_h^l$ from Eq. (9) into Eq. (11) to give

$$\widetilde{B}_h(x_1, r_x) = \int_{S_{(y_1 = L_h^-)}} \left(2\mathrm{i}k\bar{M}_h \widetilde{G}_h^l \widetilde{B}\,\mathbf{i} + \widetilde{G}_h^l \frac{\partial \widetilde{B}}{\partial y_1}\,\mathbf{i} - \widetilde{B}\nabla\widetilde{G}_h^l \right) \cdot \mathrm{d}\boldsymbol{s} + \int_{S_{(y_1=0^+)}} \mathrm{i}\omega \widetilde{G}_h^l \widetilde{u}_l\,\mathbf{i} \cdot \mathrm{d}\boldsymbol{s} - \int_V (\widetilde{\boldsymbol{\omega}} \times \boldsymbol{u_c}) \cdot \nabla \widetilde{G}_h^l \mathrm{d}v, \tag{18}$$

where V denotes the interior hole volume. Similar to the analysis for Eq. (12), only upstream propagating waves at the $y_1 = L_h^-,\ r_y < R_h$ surface contribute to the first integration term.

The stagnation enthalpy oscillations inside the hole can also be calculated by substituting $\widetilde{G}_h^r$ from Eq. (10) into Eq. (11) to give

$$\widetilde{B}_h(x_1, r_x) = \int_{S_{(y_1 = 0^+)}} \left(2\mathrm{i}k\bar{M}_h \widetilde{G}_h^r \widetilde{B}\,\mathbf{i} + \widetilde{G}_h^r \frac{\partial \widetilde{B}}{\partial y_1}\,\mathbf{i} - \widetilde{B}\nabla\widetilde{G}_h^r \right) \cdot \mathrm{d}\boldsymbol{s} + \int_{S_{(y_1=L_h^-)}} \mathrm{i}\omega \widetilde{G}_h^r \widetilde{u}_r\,\mathbf{i} \cdot \mathrm{d}\boldsymbol{s} - \int_V (\widetilde{\boldsymbol{\omega}} \times \boldsymbol{u_c}) \cdot \nabla \widetilde{G}_h^r \mathrm{d}v, \tag{19}$$

where only downstream propagating waves at the $y_1 = 0^+,\ r_y < R_h$ surface contribute to the first integration term. $\widetilde{u}_r$ is the unknown velocity oscillation at the hole outlet surface which can be expanded as a sum of a series of Bessel functions

$$\widetilde{u}_r = \sum_{m=0}^{+\infty} U_{rm} J_0(j_m r_y / R_h). \tag{20}$$

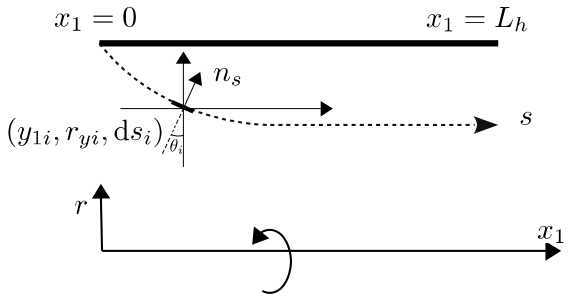

Figure 4: Discretized vortex sheet inside the hole

The shedding of the vortex sheet from the front lip of the hole and its subsequent convection downstream is shown diagrammatically in Fig. 4. The vortex sheet strength can then be written as

$$\widetilde{\boldsymbol{\omega}} = \sigma e^{\mathrm{i}k_0 s}\delta(n_s)\mathbf{k}, \tag{21}$$

where σ denotes the value of the shed vorticity at the edge, $k_0 = \omega/U_c$ the vortex convection wave number with the vortex convection velocity U_c assumed equal to the mean velocity inside the hole, $s \geq 0$ the distance from the inlet edge along the path of the vortex sheet, δ the Dirac delta function, n_s the coordinate in the normal direction of the vortex sheet and $\mathbf{k}$ a unit vector in the azimuthal direction. If the vortex sheet marks out a straight downstream path with constant radius, as assumed by Howe [8], the volume integration in Eqs. (18) and (19) can be calculated analytically. However, the mean flow contraction in reality gives a curved vortex sheet shape near the hole inlet edge as shown in Fig. 4. To calculate the vortex induced oscillations (corresponding to the volume integration in Eqs. (18) and (19)), the curved vortex sheet is discretized along its path into N_v short truncated cone rings in which y_{1i}, r_{yi}, s_i, $\mathrm{d}s_i$ denote the axial position, radius, vortex path position, and length along the vortex path of the ith ring respectively. θ_i is the angle between the ith vortex ring normal direction and the hole radial direction. The vortex induced oscillations in Eqs. (18) and (19) can be written as the sum of the contributions from all the discretized rings. Oscillations near the hole inlet (with $y_1 > x_1 \sim 0^+$) can then be written as :

$$\begin{aligned} -\int_V (\widetilde{\boldsymbol{\omega}} \times \boldsymbol{u_c}) \cdot \nabla \widetilde{G}_h^l \mathrm{d}v &= -\iint \sigma U_c \Big(\frac{\partial \widetilde{G}_h^l}{\partial r_y} \cos\theta + \frac{\partial \widetilde{G}_h^l}{\partial y_1} \sin\theta \Big) \delta(n_s) e^{\mathrm{i}k_0 s} 2\pi r_y \mathrm{d}r_y \mathrm{d}y_1 \\ &= \sigma U_c \sum_{n=0}^{+\infty} \frac{\mathrm{i}J_0(j_n r_x/R_h)}{R_h^2 J_0^2(j_n)\gamma_h^{(n)}} \Big(e^{\mathrm{i}k_h^{n-} x_1} - \frac{k_h^{n-}}{k_h^{n+}} e^{\mathrm{i}k_h^{n+} x_1} \Big) S_{dl}^{(n)}, \end{aligned} \tag{22}$$

where

$$S_{dl}^{(n)} = \sum_{i=1}^{N_v} \Big(\frac{j_n \cos\theta_i}{R_h} J_1(\frac{j_n r_{yi}}{R_h}) + \mathrm{i}k_h^{n-} J_0(\frac{j_n r_{yi}}{R_h}) \sin\theta_i \Big) e^{\mathrm{i}(k_0 s_i - k_h^{n-} y_{1i})} r_{yi} \mathrm{d}s_i$$

denotes the sum of all the vortex rings. Oscillations near the hole outlet (with $y_1 < x_1 \sim L_h^-$) can similarly be written as

$$-\int_V (\widetilde{\boldsymbol{\omega}} \times \boldsymbol{u_c}) \cdot \nabla \widetilde{G}_h^r \mathrm{d}v = \sigma U_c \sum_{n=0}^{+\infty} \frac{\mathrm{i}J_0(j_n r_x/R_h)}{R_h^2 J_0^2(j_n)\gamma_h^{(n)}} \Big(e^{\mathrm{i}k_h^{n+}(x_1 - L_h)} - \frac{k_h^{n+}}{k_h^{n-}} e^{\mathrm{i}k_h^{n-}(x_1 - L_h)} \Big) S_{dr}^{(n)}, \tag{23}$$

where

$$S_{dr}^{(n)} = \sum_{i=1}^{N_v} \Big(\frac{j_n \cos\theta_i}{R_h} J_1(\frac{j_n r_{yi}}{R_h}) + \mathrm{i}k_h^{n+} J_0(\frac{j_n r_{yi}}{R_h}) \sin\theta_i \Big) e^{\mathrm{i}(k_0 s_i - k_h^{n+}(y_{1i} - L_h))} r_{yi} \mathrm{d}s_i.$$

Next, we write the overall downstream and upstream propagating waves inside the hole as

$$\widetilde{B}_h^+ = \sum_{m=0}^{+\infty} \widetilde{B}_h^{m+} e^{\mathrm{i}k_h^{m+}x_1} J_0(j_m r_x/R_h), \tag{24}$$

$$\widetilde{B}_h^- = \sum_{m=0}^{+\infty} \widetilde{B}_h^{m-} e^{\mathrm{i}k_h^{m-}(x_1-L_h)} J_0(j_m r_x/R_h). \tag{25}$$

Substituting Eqs. (14), (22) and (25) into Eq. (18) gives the wave strength near the hole inlet ($x_1 \sim 0^+$) as

$$\begin{aligned}\widetilde{B}_h(x_1 \sim 0^+, r_x) = &\sum_{m=0}^{+\infty} \widetilde{B}_h^{m-} e^{-\mathrm{i}k_h^{m-}L_h}\Big(e^{\mathrm{i}k_h^{m-}x_1} - \frac{k_h^{m-}}{k_h^{m+}} e^{\mathrm{i}k_h^{m+}x_1}\Big) J_0(j_m r_x/R_h) + \omega \sum_{m=0}^{+\infty} \frac{U_{lm} J_0(j_m r_x/R_h)}{k_h^{m+}} e^{\mathrm{i}k_h^{m+}x_1} \\ &+\sigma U_c \sum_{m=0}^{+\infty} \frac{\mathrm{i} J_0(j_m r_x/R_h)}{R_h^2 J_0^2(j_n)\gamma_h^{(m)}}\Big(e^{\mathrm{i}k_h^{m-}x_1} - \frac{k_h^{m-}}{k_h^{m+}} e^{\mathrm{i}k_h^{m+}x_1}\Big) S_{dl}^{(m)}.\end{aligned} \tag{26}$$

While substituting Eqs. (20), (23) and (24) into Eq. (19) gives the wave strength near the hole outlet ($x_1 \sim L_h^-$) as

$$\begin{aligned}\widetilde{B}_h(x_1 \sim L_h^-, r_x) = &\sum_{m=0}^{+\infty} \widetilde{B}_h^{m+} e^{\mathrm{i}k_h^{m+}L_h}\Big(e^{\mathrm{i}k_h^{m+}(x_1-L_h)} - \frac{k_h^{m+}}{k_h^{m-}} e^{\mathrm{i}k_h^{m-}(x_1-L_h)}\Big) J_0(j_m r_x/R_h) + \omega \sum_{m=0}^{+\infty} \frac{U_{rm} J_0(j_m r_x/R_h)}{k_h^{m-}} e^{\mathrm{i}k_h^{m-}(x_1-L_h)} \\ &+\sigma U_c \sum_{m=0}^{+\infty} \frac{\mathrm{i} J_0(j_m r_x/R_h)}{R_h^2 J_0^2(j_m)\gamma_h^{(m)}}\Big(e^{\mathrm{i}k_h^{m+}(x_1-L_h)} - \frac{k_h^{m+}}{k_h^{m-}} e^{\mathrm{i}k_h^{m-}(x_1-L_h)}\Big) S_{dr}^{(m)}.\end{aligned} \tag{27}$$

By comparing Eqs. (24) and (26), and (25) and (27), the following relations can be obtained:

$$\widetilde{B}_h^{m+} = \frac{\omega U_{lm}}{k_h^{m+}} - \frac{\mathrm{i}\sigma U_c k_h^{m-} S_{dl}^{(m)}}{R_h^2 J_0^2(j_n)\gamma_h^{(m)} k_h^{m+}} - \widetilde{B}_h^{m-} e^{-\mathrm{i}k_h^{m-}L_h} \frac{k_h^{m-}}{k_h^{m+}}, \tag{28}$$

$$\widetilde{B}_h^{m-} = \frac{\omega U_{rm}}{k_h^{m-}} - \frac{\mathrm{i}\sigma U_c k_h^{m+} S_{dr}^{(m)}}{R_h^2 J_0^2(j_n)\gamma_h^{(m)} k_h^{m-}} - \widetilde{B}_h^{m+} e^{\mathrm{i}k_h^{m+}L_h} \frac{k_h^{m+}}{k_h^{m-}}. \tag{29}$$

Finally Eqs. (28) and (29) can be combined to obtain the amplitudes of the up- and downstream propagating waves:

$$\widetilde{B}_h^{m+} = \frac{1}{1 - e^{2\mathrm{i}\gamma_h^{(m)}L_h}}\Big[\frac{\omega}{k_h^{m+}}(U_{lm} - U_{rm}e^{-\mathrm{i}k_h^{m-}L_h}) - \frac{\mathrm{i}\sigma U_c}{\gamma_h^{(m)} R_h^2 J_0^2(j_m)}\Big(\frac{k_h^{m-}}{k_h^{m+}} S_{dl}^{(m)} - e^{-\mathrm{i}k_h^{m-}L_h} S_{dr}^{(m)}\Big)\Big], \tag{30}$$

$$\widetilde{B}_h^{m-} = \frac{1}{1 - e^{2\mathrm{i}\gamma_h^{(m)}L_h}}\Big[\frac{\omega}{k_h^{m-}}(U_{rm} - U_{lm}e^{\mathrm{i}k_h^{m+}L_h}) - \frac{\mathrm{i}\sigma U_c}{\gamma_h^{(m)} R_h^2 J_0^2(j_m)}\Big(\frac{k_h^{m+}}{k_h^{m-}} S_{dr}^{(m)} - e^{\mathrm{i}k_h^{m+}L_h} S_{dl}^{(m)}\Big)\Big]. \tag{31}$$

2.2.3. Oscillations downstream of the hole

At the downstream region of the hole outlet, since it is assumed that no waves arrive from the far downstream, substituting the downstream Green's function Eq. (8) into Eq. (11) reveals that only the vortex sheet inside the downstream part and the velocity oscillations at the hole outlet surface contribute to the stagnation enthalpy oscillations. The contribution from the hole outlet velocity oscillations can be similarly calculated by using the same method used at the upstream region of the hole inlet (see Eq. (15)).

For the shape of the vortex sheet, a fully contracted semi-infinitely long vortex cylinder is used if the hole length is larger than half its radius (the mean flow can be assumed to be fully contracted after approximately this length [16]), but not long enough to allow the vortex sheet to reattach the hole inside wall. For shorter holes, a curved vortex shape needs to be considered and the same discretization method shown in Eqs. (22) and (23) can be used again.

If the downstream vortex sheet is fully contracted and can be assumed to be a semi-infinitely long cylinder with constant radius R_v ($< R_h$), the vortex contributions to the oscillations can be obtained by calculating the volume

integration in Eq. (11) directly (without discretization). Oscillations at the downstream region of the hole outlet can thus be written as

$$\begin{aligned}\widetilde{B}_d(x_1, r_x) =& \int_{S_{(y_1=L_h^+)}} \mathrm{i}\omega \widetilde{G}_d \widetilde{u}_r \,\mathbf{i}\cdot \mathrm{d}\boldsymbol{s} - \int_V (\widetilde{\boldsymbol{\omega}}\times \boldsymbol{u_c})\cdot\nabla\widetilde{G}_d \mathrm{d}v \\ =& 2\omega \sum_{m=0}^{+\infty} U_{rm} e^{\mathrm{i}k_d^{m+}(x_1-L_h)} \sum_{n=0}^{+\infty} \frac{\int_0^1 J_0(j_n r_y^*/\lambda_d) J_0(j_m r_y^*) r_y^* \mathrm{d}r_y^*}{k_d^{n+}\lambda_d^2 J_0^2(j_n)} J_0(j_n r_x/R_d) \\ &+ 2\sigma U_c e^{\mathrm{i}k_0\Delta s} \sum_{n=0}^{+\infty} \frac{J_1(j_n R_v/R_d) R_v j_n J_0(j_n r_x/R_d)}{R_d^3 J_0^2(j_n)(k_0-k_d^{n-})(k_0-k_d^{n+})k_d^{n+}} \Big(k_d^{n+} e^{\mathrm{i}k_0(x_1-L_h)} - k_0 e^{\mathrm{i}k_d^{n+}(x_1-L_h)}\Big),\end{aligned} \tag{32}$$

where Δs denotes the distance along the vortex path from the hole inlet edge to the hole outlet surface.

2.3. Calculating the vortex strength and the hole impedance

Having obtained full expressions for the stagnation enthalpy oscillations near the hole inlet and outlet surfaces, the oscillating velocity at the hole inlet ($\widetilde{u}_l$) and outlet ($\widetilde{u}_r$) can be calculated by using the condition that the stagnation enthalpy oscillation across these two surfaces are both continuous. The vortex shedding strength is determined by applying the Kutta condition at the hole inlet edge.

The stagnation enthalpy oscillation continuity can be written as

$$\widetilde{B}_u(x_1 = 0^-, r_x) = \widetilde{B}_h(x_1 = 0^+, r_x), \tag{33}$$

$$\widetilde{B}_h(x_1 = L_h^-, r_x) = \widetilde{B}_d(x_1 = L_h^+, r_x). \tag{34}$$

Substituting Eqs. (16), (26) and (31) into (33), multiplying by $J_0(j_p r_x/R_h) r_x$ on both sides ($p = 0, 1, 2, 3, \ldots P-1$) and integrating from 0 to R_h with respect to r_x gives P equations (noting the orthogonality of Bessel functions [25])

$$Y_u(p+1) = \sum_{m=0}^{+\infty} \mathcal{M}_{11}(p+1, m+1) U_{lm} + \sum_{m=0}^{+\infty} \mathcal{M}_{12}(p+1, m+1) U_{rm} + \sigma Y_{hl}(p+1). \tag{35}$$

Here $Y_u(p+1) = \widetilde{B}_{u0}^+ \delta_{p0}/(1+\bar{M}_u)$ and is non-zero only when $p = 0$,

$$Y_{hl}(p+1) = \frac{\mathrm{i}U_c}{(1-e^{2\mathrm{i}\gamma_h^{(p)}L_h})k_h^{p+}R_h^2} \Big(S_{dl}^{(p)} - e^{-\mathrm{i}k_h^{p-}L_h} \frac{k_h^{p+}}{k_h^{p-}} S_{dr}^{(p)}\Big), \tag{36}$$

$$\mathcal{M}_{11}(p+1, m+1) = \frac{\omega(k_h^{p-} - k_h^{p+} e^{2\mathrm{i}\gamma_h^{(p)}L_h}) J_0^2(j_p)}{2(1-e^{2\mathrm{i}\gamma_h^{(p)}L_h})k_h^{p+}k_h^{p-}} \delta_{mp} - \sum_{n=0}^{+\infty} \frac{2\omega I_u^{pn} I_u^{mn}}{k_h^{n-}\lambda_u^2 J_0^2(j_n)}, \tag{37}$$

$$\mathcal{M}_{12}(p+1, m+1) = \frac{\omega e^{-\mathrm{i}k_h^{p-}L_h} \gamma_h^{(p)} J_0^2(j_p)}{(1-e^{2\mathrm{i}\gamma_h^{(p)}L_h})k_h^{p+}k_h^{p-}} \delta_{mp}, \tag{38}$$

where $\delta_{mp} = 1$ if $m = p$ and 0 if $m \neq p$, $I_u^{pn} = \int_0^1 J_0(j_n r^*/\lambda_u) J_0(j_p r^*) r^* \mathrm{d}r^*$ and $I_u^{mn} = \int_0^1 J_0(j_n r^*/\lambda_u) J_0(j_m r^*) r^* \mathrm{d}r^*$.

Similarly, substituting Eqs. (27) (30) and (32) into (34), multiplying both sides by $J_0(j_p r_x/R_h) r_x$ ($p = 0, 1, 2, 3, \ldots P-1$) and integrating from 0 to R_h with respect to r_x gives another P equations

$$-\sigma Y_d(p+1) = \sum_{m=0}^{+\infty} \mathcal{M}_{21}(p+1, m+1) U_{lm} + \sum_{m=0}^{+\infty} \mathcal{M}_{22}(p+1, m+1) U_{rm} - \sigma Y_{hr}(p+1), \tag{39}$$

where

$$Y_d(p+1) = -2U_c e^{\mathrm{i}k_0\Delta s} \int_0^1 \sum_{n=0}^{+\infty} \frac{J_1(j_n R_v/R_d) R_v j_n J_0(j_n r^*/\lambda_d)}{R_d^3 J_0^2(j_n)(k_0-k_d^{n-})k_d^{n+}} J_0(j_p r^*) r^* \mathrm{d}r^*, \tag{40}$$

$$Y_{hr}(p+1) = \frac{-\mathrm{i}U_c}{(1-e^{2\mathrm{i}\gamma_h^{(p)}L_h})k_h^{p-}R_h^2}\left(S_{dr}^{(p)} - e^{\mathrm{i}k_h^{p+}L_h}\frac{k_h^{p-}}{k_h^{p+}}S_{dl}^{(p)}\right), \tag{41}$$

$$\mathcal{M}_{21}(p+1,m+1) = \frac{\omega e^{\mathrm{i}k_h^{p+}L_h}\gamma_h^{(p)}J_0^2(j_p)}{(1-e^{2\mathrm{i}\gamma_h^{(p)}L_h})k_h^{p+}k_h^{p-}}\delta_{mp}, \tag{42}$$

$$\mathcal{M}_{22}(p+1,m+1) = \frac{\omega(k_h^{p-}e^{2\mathrm{i}\gamma_h^{(p)}L_h} - k_h^{p+})J_0^2(j_p)}{2(1-e^{2\mathrm{i}\gamma_h^{(p)}L_h})k_h^{p+}k_h^{p-}}\delta_{mp} + \sum_{n=0}^{+\infty}\frac{2\omega I_d^{pn}I_d^{mn}}{k_h^{n+}\lambda_d^2J_0^2(j_n)}, \tag{43}$$

in which $I_d^{pn} = \int_0^1 J_0(j_n r^*/\lambda_d)J_0(j_p r^*)r^*\mathrm{d}r^*$ and $I_d^{mn} = \int_0^1 J_0(j_n r^*/\lambda_d)J_0(j_m r^*)r^*\mathrm{d}r^*$.

To solve Eqs (35) and (39), the velocity series in $\widetilde{u_l}$ and $\widetilde{u_r}$ are truncated at the Mth term (which means the summations in Eqs (35) and (39) are truncated at $m = M-1$), and the up- and downstream Green's functions are truncated at the Nth term (which means the summations in $\mathcal{M}_{11}$ and $\mathcal{M}_{22}$ are truncated at $n = N-1$). It is worth noting that the value of N used (in Eq. (40)) to calculated the vortex induced oscillations at the downstream region of the hole outlet can be larger than the value of N used in other Green's functions in order to get an accurate vortex response at the downstream side of the hole outlet. This will not increase the computation much as the integration can be performed numerically after summation. By taking $P = M$, Eqs (35) and (39) can be written as

$$\boldsymbol{Y_u} - \sigma\boldsymbol{Y_{hl}} = \mathcal{M}_{11}\boldsymbol{U_l} + \mathcal{M}_{12}\boldsymbol{U_r}, \tag{44}$$

$$\sigma(\boldsymbol{Y_{hr}} - \boldsymbol{Y_d}) = \mathcal{M}_{21}\boldsymbol{U_l} + \mathcal{M}_{22}\boldsymbol{U_r}, \tag{45}$$

where $\boldsymbol{Y_u} = [Y_u(0), Y_u(1), ...Y_u(M-1)]^T$ is a M-element column vector whose ith row is $Y_u(i)$ ($\boldsymbol{Y_d}, \boldsymbol{Y_{hl}}, \boldsymbol{Y_{hr}}$ are defined in the same way), $\boldsymbol{U_l} = [U_{l0}, U_{l1}, ...U_{l(M-1)}]^T$ is a M-element column vector whose ith row is U_{li} ($\boldsymbol{U_r}$ is defined in the same way), $\mathcal{M}_{11}, \mathcal{M}_{12}, \mathcal{M}_{21}, \mathcal{M}_{22}$ are all $M \times M$ matrix.

The Kutta condition requires $\widetilde{u_l}$ to be zero at the hole inlet edge ($y_1 = 0, r_y = R_h$), which means

$$\sum_{m=0}^{M-1} U_{lm}J_0(j_m) = 0. \tag{46}$$

By combining Eqs. (44), (45) and (46), the vortex strength can be obtained as

$$\sigma = \frac{[(\mathcal{M}_{11} - \mathcal{M}_{12}\mathcal{M}_{22}^{-1}\mathcal{M}_{21}) \setminus \boldsymbol{Y_u}] \cdot \boldsymbol{Y_R}}{[(\mathcal{M}_{11} - \mathcal{M}_{12}\mathcal{M}_{22}^{-1}\mathcal{M}_{21}) \setminus (\boldsymbol{Y_{hl}} + \mathcal{M}_{12}\mathcal{M}_{22}^{-1}(\boldsymbol{Y_{hr}} - \boldsymbol{Y_d}))] \cdot \boldsymbol{Y_R}} \tag{47}$$

where $\mathcal{M}_{22}^{-1}$ is the inverse matrix of $\mathcal{M}_{22}$, $\setminus$ means solving linear matrix equations (e.g. $\boldsymbol{x} = M_{atrix} \setminus \boldsymbol{y}$ is the solution of $M_{atrix}\boldsymbol{x} = \boldsymbol{y}$) and $\boldsymbol{Y_R} = [J_0(j_0), J_0(j_1), ...J_0(j_{(M-1)})]^T$. Substituting the vortex strength back into Eqs. (44), (45), the velocities can be obtained through

$$\boldsymbol{U_l} = (\mathcal{M}_{11} - \mathcal{M}_{12}\mathcal{M}_{22}^{-1}\mathcal{M}_{21}) \setminus (\boldsymbol{Y_u} - \sigma\boldsymbol{Y_{hl}} + \sigma\mathcal{M}_{12}\mathcal{M}_{22}^{-1}(\boldsymbol{Y_d} - \boldsymbol{Y_{hr}})), \tag{48}$$

$$\boldsymbol{U_r} = -\mathcal{M}_{22}^{-1}\sigma(\boldsymbol{Y_d} - \boldsymbol{Y_{hr}}) - \mathcal{M}_{22}^{-1}\mathcal{M}_{21}\boldsymbol{U_l}. \tag{49}$$

Substituting U_{l0}, the first term in $\boldsymbol{U_l}$, into Eq. (17), both the down- and upstream propagating waves can be obtained as a function of $\widetilde{B}_{u0}^+$ – the incident wave from upstream. As the flow is irrotational, the oscillating axial velocity can be obtained from stagnation enthalpy oscillation, $\mathrm{i}\omega\widetilde{u} = \partial\widetilde{B}/\partial x_1$, and the oscillating pressure from $\widetilde{p} = (\widetilde{B} - \bar{u}\widetilde{u})\bar{\rho}$. Thus, the impedance ahead of the hole inlet (close to the hole inlet when considering the plane wave but far enough to ignore any high-order modes) can be written as

$$Z_u = \frac{\widetilde{p}}{\widetilde{u}} = \frac{\bar{\rho}(\mathrm{i}\omega\widetilde{B} - \bar{u}\partial\widetilde{B}/\partial x_1)}{\partial\widetilde{B}/\partial x_1} = \bar{\rho}\bar{c}\frac{(2\widetilde{B}_{u0}^+/(1+\bar{M}_u) - U_{l0}\bar{c}/\lambda_u^2)}{U_{l0}\bar{c}/\lambda_u^2}. \tag{50}$$

As the whole system is linear, $\widetilde{B}_{u0}^+$ is arbitrary and $\widetilde{B}_{u0}^+ = 1$ can be used. It should be noted that the impedance at the hole inlet surface (Z_{hl}) can be easily calculated – the pressure is the same as that just before the inlet but the velocity is λ_u^2 times that before it, and so $Z_{hl} = Z_u/\lambda_u^2$.

3. Results for short holes

Consider the geometry shown in Fig. 1 with parameters $R_h = 0.006\ m$, $L_h/D = 0.5$ ($D = 2R_h$ is the hole diameter) and $\bar{M}_h = 0.062$. Room temperature $T = 290\ K$ and pressure $P = 10^5\ Pa$ are considered. The frequency is normalized by introducing the Strouhal number

$$S_t = \frac{\omega R_h}{U_c}. \tag{51}$$

3.1. Convergence and validation

A convergence check on the truncation numbers for the velocity expansion (M) and the Green's functions up- and downstream (N) is firstly performed. The radius expansion ratios up- and downstream of the hole are both chosen to be $\lambda_u = \lambda_d = \lambda = 30$. $S_t = 0.9$ is taken as an illustrative example. The predicted impedance shown in Fig. 5 is clearly seen to converge with increasing M and N, with $M = 500$ and $N = 5000$ large enough for converged predictions. It is worth noting that if a smaller expansion ratio is used, a much smaller truncation number would be required.

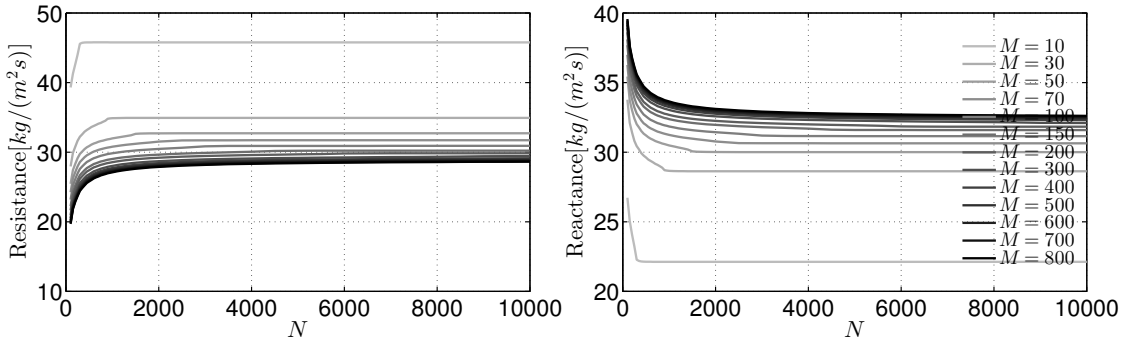

Figure 5: The convergence of the impedance with the truncation numbers of the velocity oscillations (M) and Green's functions (N). $S_t = 0.9$.

Choosing $\lambda_u = \lambda_d = \lambda = 30$ ensures that the expansion ratio is large enough for results to be independent of the expansion ratio. To check this, the impedance is calculated with $M = 500$ and $N = 5000$ but various expansion ratios. Figure (6) shows that resistance and reactance both vary strongly with expansion ratio for values below 10, but can be considered converged with expansion ratio for $\lambda > 30$.

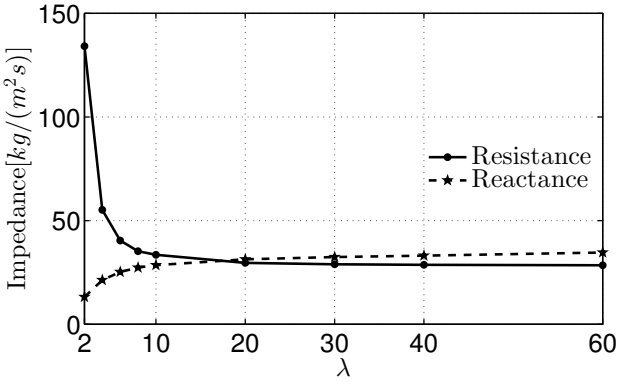

Figure 6: The convergence of the impedance with the radius expansion ratio λ ($= \lambda_u = \lambda_d$). $S_t = 0.9$.

A confirmation of expansion ratio convergence can be achieved by comparing the predicted shed vorticity and Rayleigh conductivity, $K_R = 2R_h(\Gamma_R - \mathrm{i}\Delta_R)$, with Howe's model [8] in the zero hole length limit. As Howe's model assumes zero hole length and a cylindrical vortex sheet with the same radius as the hole, the same assumptions are used here. Howe's model assumes infinitely large half spaces either side of the hole; this cannot be achieved by the present

model and at high expansion ratio errors will be introduced near the large-cylinder higher mode cut-on frequencies. Instead, predictions for expansion ratios varying from $\lambda = 0.5$ to $\lambda = 30$ are shown. The comparison of the strength and phase of the shed vortex sheet is shown in Fig. 7 (top), with good agreement in strength prediction across all Strouhal numbers at $\lambda = 30$. Improving the phase prediction, especially at higher frequencies would require higher expansion ratios and velocity expansion truncation number, which would introduce errors near the cut-on frequencies of the large cylinders. Figure 7 (bottom) compares the Rayleigh conductivities of the present and Howe's models, showing that $\lambda = 30$ is sufficiently large to yield a very similar plane acoustic response to Howe's model over the relevant frequencies.

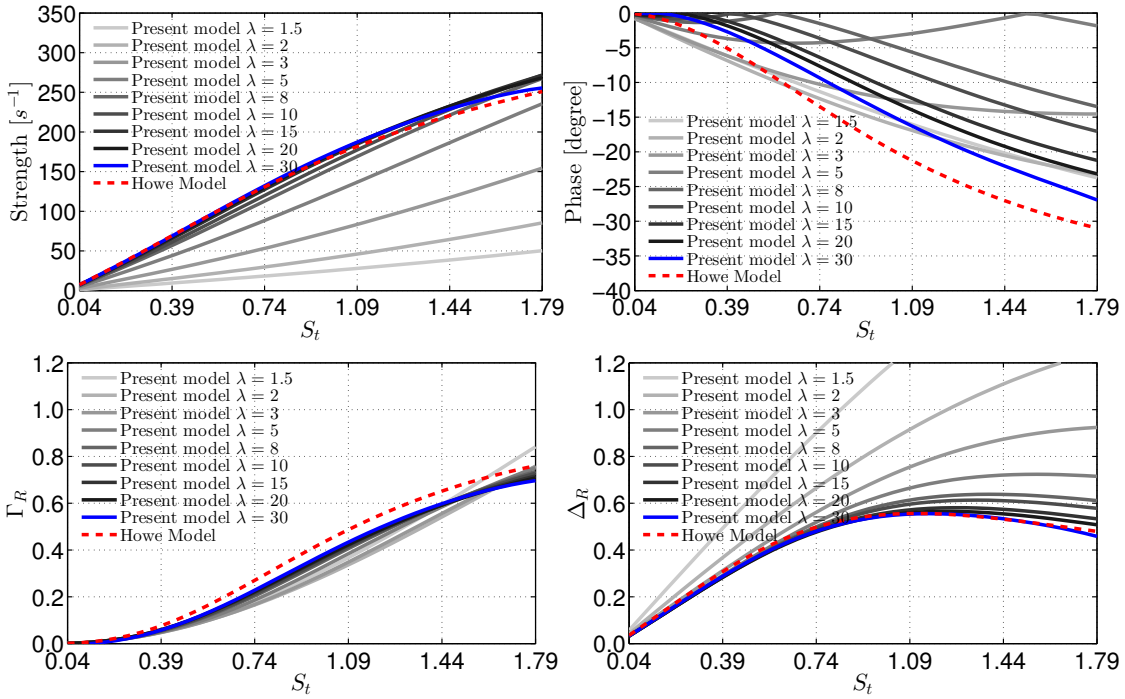

Figure 7: The strength and phase of the vortex sheet (σ) shed from the lip of an infinitesimally short hole (top) and the real and imaginary parts of its corresponding Rayleigh conductivity $K_R = 2R_h(\Gamma_R - i\Delta_R)$ (bottom).

It is worth noting that all the calculations shown in this article can be performed on a general PC in very little time, other than calculation of the integrations I_u^{pn} and I_d^{pn}, which may take several to ten or twenty minutes depending on the truncation numbers. As I_u^{pn} and I_d^{pn} vary only with the radius expansion ratio (λ), which has been shown to have little affect once larger than 30, any larger expansion ratios can be treated as 30 (at least in the low Strouhal number region considered here). For smaller expansion ratios, the required truncation numbers M and N decrease rapidly, accompanied by a reduction in the computational time for I_u^{pn} and I_d^{pn}. Finally, even though direct calculations are not that time consuming, it may be more convenient to build a database for I_u^{pn} and I_d^{pn} at different expansion ratios. Then, all calculations related to this model can be performed on a general PC in very little time.

3.2. Comparison with experiments, CFD and other models

The acoustic impedances of short finite length holes at low Strouhal numbers (frequencies) are now calculated and compared with results from experiments, CFD and some other widely used models.

For a hole with length to diameter ratio $L_h/D = 0.5$, experimental and CFD results were recently published [15]. Our impedance predictions are compared to these, along with predictions from other methods, in Fig. 8. All of the models predict a nearly constant resistance at very low Strouhal number ($S_t < 0.4$), in agreement with experimental measurements and CFD results. However, both Bellucci's model [3] and Howe's model with an inertial length correction predict almost constant resistance as Strouhal number increases ($0.4 < S_t < 1.79$), while the experiments

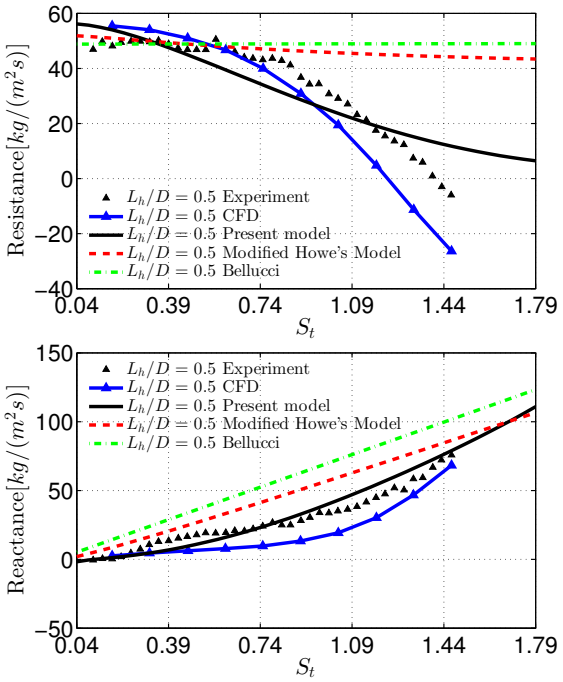

Figure 8: Impedance comparison for the case $R_h = 0.006\ m$, $L_h/D = 0.5$, $\bar{M}_h = 0.062$. The Reynolds number based on the hole diameter is approximately 16000. Experimental and CFD results from Su et al. [15], the Modified Howe's Model [8] applies a compact hole mass inertial correction from [10], Bellucci's semi-empirical model [3] uses the measured discharge coefficient from [15].

and CFD indicate a dramatic decrease in resistance, even to negative values. It is clearly seen that only the CFD simulation and the present analytical model are able to capture this significant decrease. The difference between the present model and the experimental and CFD results may mainly arise from differences in the vortex sheet shapes – the impact of these will be discussed in detail later. For the reactance, both Bellucci's model and the improved Howe's model predict a linear increase, while the experiment shows a nonlinear increase, faster at higher Strouhal numbers. Again, only the CFD simulation and the present analytical model predict this trend.

3.3. Impact of the hole length to diameter ratio

Although the model developed in this paper predicts the correct trend for the variation of the resistance with frequency, it does not capture the full extent of the decrease, including to negative values at higher frequencies. This is consistent with Jing and Sun's [14] prediction from a boundary element method, in which they found that the hole length to diameter ratio needs to be larger than 0.75 ($L_h/D > 0.75$) in order to obtain a negative resistance regime.

Figure 9 shows impedance predictions from the present model for the same case as that shown in Fig. 8 with only the exception that a larger range of hole length to diameter ratios is shown. It is clear that the resistance decreases to negative values can be predicted for hole length to diameter ratios exceeding about 0.75. The negative region moves towards lower Strouhal numbers as the length to diameter ratio increases, likely to be explained by the coupling frequency between the hole inlet and outlet reducing for longer holes. At low Strouhal numbers ($S_t < 0.4$), the reactance is seen to depend little on the hole length to diameter ratio – the hole is almost compact, with the reactance small and mainly determined by the sound radiation either side of the hole. The reactance increase with frequency ($S_t > 0.4$) is more pronounced for higher length to diameter ratios. This is for two reasons: the inertial effect of the mass inside the hole becomes important as length increases, and furthermore the effect of the coupling between the shed vorticity and the acoustic wave strengths inside the hole also increases with hole length. The former effect has been widely accounted for [2, 10, 11] by adding a mass inertial correction term to Howe's model for an infinitesimally short hole [8]. The latter effect has been seen both experimentally and numerically by several researchers [14, 15, 26].

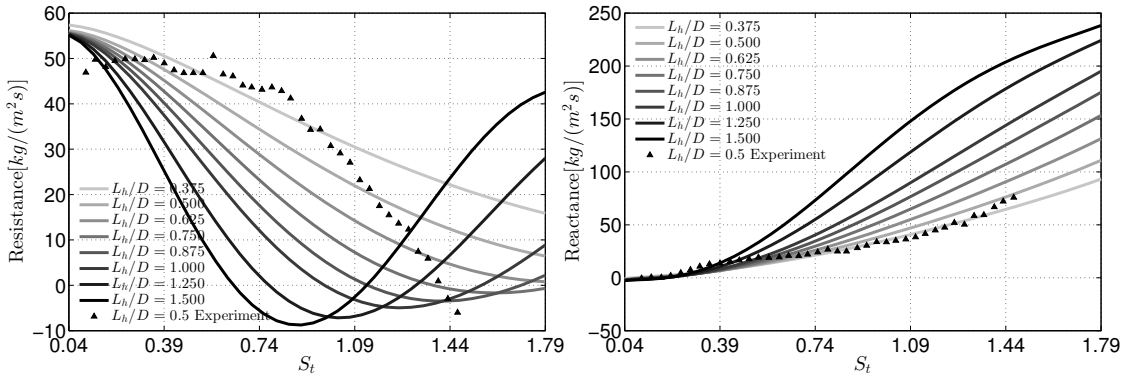

Figure 9: Impedance variation with hole length diameter ratio. Predicted by the present model.

This acoustic-vortex coupling is captured by the present analytical model and the effect of this can be clearly seen in the improved impedance prediction from the present model compared to the simpler models in Fig. 8.

3.4. Impact of the vortex sheet shape

In the present model, the experimentally measured vortex sheet profile [16] for a hole opening towards semi-infinite spaces on both sides is used. This shape was used by Jing and Sun in their boundary element method model [14] and both the vortex sheet shape near the hole inlet edge and the corresponding impedance for a $L_h/D = 0.25$ case was validated by Mendez and Eldrege [26] using a LES code. However, it is widely known that both the flow contraction coefficient – the minimum vortex sheet radius divided by the hole radius – and the vortex sheet shape near the inlet edge are very sensitive to the upstream hole expansion ratio [16], the hole inlet edge sharpness and the flow Reynolds number [27–29]. It is important to know whether the difference between the vortex sheet shape encountered in practice and the idealized vortex sheet shape (e.g. for an idealized sharp edge, infinitely large expansion and high Reynolds number) will change the hole impedance greatly. In the following part of this section, it will be shown that the vortex sheet contraction coefficient and the exact vortex sheet shape near the hole inlet edge are important in affecting the vortex shedding at the edge and thus the overall hole impedance.

Figure 10 shows the experimentally measured vortex sheet shape from [16] which we choose to model using an exponential function of the form

$$y^* = 1 - a(1 - e^{-bx^*}), \tag{52}$$

where $y^* = R_V/R_h$ and $x^* = x_1/R_h$. Figure 10 shows that $a = 0.2,\ b = 6$ gives approximately the same shape as the experimental result. Changing the values of a and b changes the vortex sheet shape, as seen in Fig. 10.

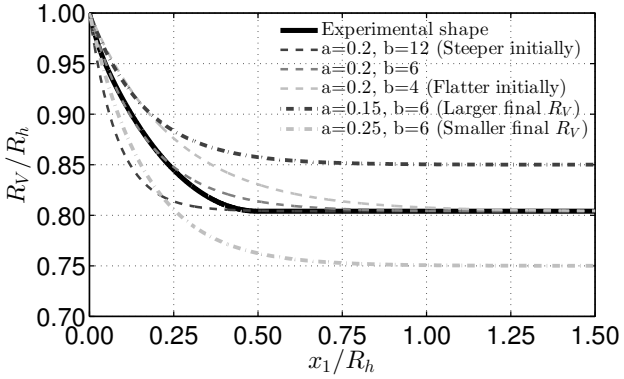

Figure 10: Experimental and several fitted vortex sheet shapes as a function of the axial distance (at downstream) to the hole inlet surface.

Figure 11 shows that for the same vortex sheet contraction coefficient, a steeper vortex sheet shape (a larger b) near the shedding edge gives a smaller resistance reduction and a less curved reactance with increasing frequency. On the other hand, the effect of decreasing the vortex sheet radius (increasing a), is shown in Fig. 12, with a similar impact on both the resistance and reactance as a steeper vortex sheet.

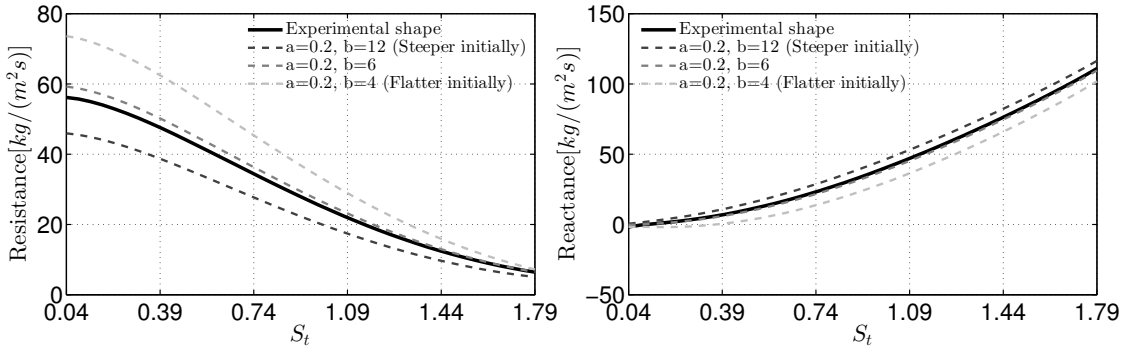

Figure 11: Impedance variation with S_t for different vortex sheet shapes near the hole inlet.

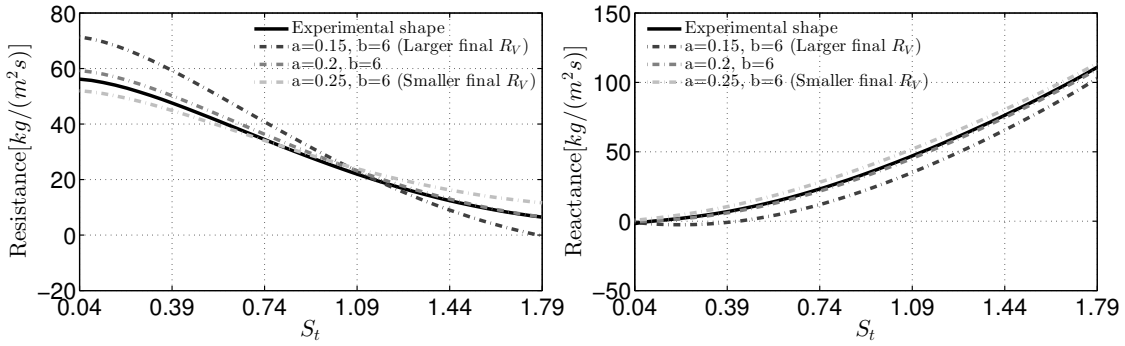

Figure 12: Impedance variation with S_t for different vortex sheet contraction ratios.

An explanation is now provided. It is clear from Fig. 8 that the resistance decrease and the nonlinear reactance dependence on frequency are the main differences in the predictive capability of the present model compared to previous models. This is due to its ability to consider the hole length and capture the exact vortex shape when calculating the shed vorticity. When applying the Kutta condition, velocity singularities generated by the incident acoustic wave and vortex sheet cancel one another. The vortex sheet induces velocity oscillations near the hole inlet edge comprising many radial modes, from which only the plane wave contributes to the main acoustic wave propagating within the finite long hole. Thus, when the acoustic feedback from the hole outlet is being considered, the upstream propagating plane acoustic wave within the hole is likely to affect the vortex shedding at the front lip of the hole more strongly when the vortex sheet contribution to the velocity singularity has a large contribution from the 0th-order mode. Both a flatter vortex sheet shape near the edge and increased final vortex sheet radius reduce the contribution from high order modes. Then it is easy to understand that increasing the initial vortex sheet steepness and reducing the final vortex sheet radius both tend to reduce the resistance fall-off and the reactance curvature with the frequency.

3.5. Possible simplifications of the present model

In many practical applications, the mean flow Mach numbers inside and either side of the hole are small, in which case their effect on the acoustic propagation can be neglected, although their effect on the convection of the shed vortices should be retained. The hole impedance at various (low) mean flow Mach numbers is compared using

predictions which account for and neglect the effect of convection on the acoustic propagation in Fig. 13. For $\bar{M}_h < 0.1$, both the resistance and reactance are largely unaffected by the mean flow influence on acoustic wave propagation. At higher Mach numbers, there is a noticeable difference, and so the effect of the mean flow on the acoustic wave propagation should be retained. Thus at very low Mach numbers, the mean flow effect on the acoustic propagation can be neglected, which involves setting $\bar{M}_u$, $\bar{M}_h$ and $\bar{M}_d$ to zero in all of the Green's functions in Eqs. (7, 8, 9, 10) and setting $\bar{M} = 0$ in Eq. (11). The final expressions for the vortex shedding, velocity oscillations at hole inlet and outlet interfaces, and the impedance for the hole are the same as those shown in Eq. (47,48,49,50) respectively, except that $\bar{M}_u$, $\bar{M}_h$ and $\bar{M}_d$ are all zero with the mean flow effect considered only in the vortex convection wave number k_0.

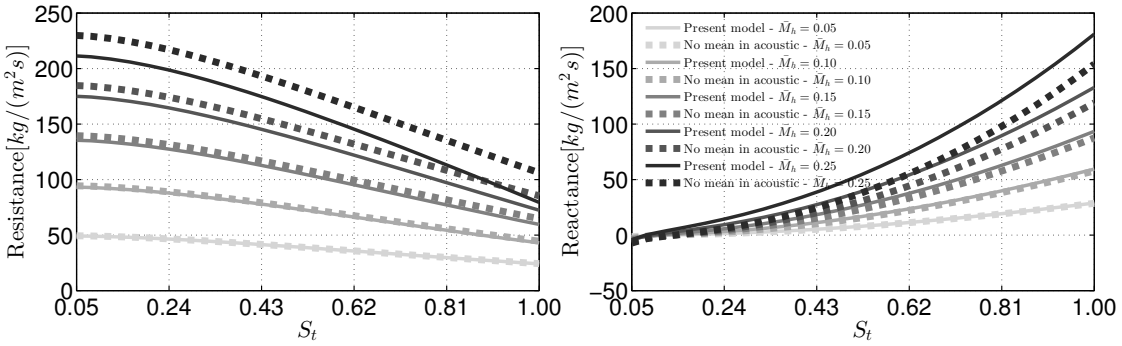

Figure 13: Impedance variation with S_t for different mean flow Mach numbers inside the hole. The solid lines denote the present model which considers the mean flow effect in both the vortex convection and the acoustic wave propagation while the dotted lines ignores the mean flow affection on the acoustic wave propagation.

Another possible simplification is to neglect the propagation of high-order acoustic waves inside the hole, allowing only plane acoustic waves to propagate between the hole inlet and outlet interfaces. This at first appears reasonable as the frequencies considered are far lower than the first cut-on frequency of the hole and thus any high-order waves damp quickly – they need to be considered only when the hole is extremely short. However, high-order oscillations near the inlet ($x_1 = 0^+$) and outlet ($x_1 = L_h^-$) interfaces must be retained to obtain the correct plane wave reflections at these two ends, and so even if only plane waves are able to propagate inside the hole, the need to account for the interface oscillations makes the calculation effort similar to that of taking all modes into consideration.

For generality and strictness, both mean flow Mach numbers and high-order acoustic wave propagation inside the hole are retained in the present model. However, it may be justified and should be straightforward for readers to use the assumptions discussed here to simplify the derivation process according to their specific applications.

4. A simplified model for long holes

The model developed so far in the paper pertains to short holes, for which the separated flow from the front lip (hole inlet edge) does not reattach to the inner wall of the hole before exiting. For longer holes, the mean flow separates at the front lip and then reattaches to the wall within the hole. At the hole outlet, the flow forms a jet expanding to the large downstream space. For high Reynolds numbers, it can be assumed that the action of viscosity is limited to bringing about the generation of a vortex sheet upon exit separation, in a similar manner to a hole with infinitely small length [8]. A small mass inertial correction term [10] to account for the hole length can be applied to the reactance provided by Howe's model [8].

For long holes, we now propose that it is sensible to allow plane waves to propagate inside the hole and to incorporate this into the modelling. Thus, the present model for long holes uses Howe's model [8] to account for the vortex sheet downstream of the hole outlet, and assumes one-dimensional axial propagating waves inside the hole. The hole inlet impedance can then be written as

$$Z_h = \bar{\rho}\bar{c} \cdot \frac{(\widetilde{Z}+1)e^{-i\frac{2\omega\bar{c}L_h}{\bar{c}^2-\bar{u}^2}} + (\widetilde{Z}-1)}{(\widetilde{Z}+1)e^{-i\frac{2\omega\bar{c}L_h}{\bar{c}^2-\bar{u}^2}} - (\widetilde{Z}-1)}, \tag{53}$$

where $\widetilde{Z} = \pi D^2/4 \cdot \omega/(\mathrm{i}\bar{c}K_R)$ is the impedance of a hole with infinitesimal thickness, K_R is Howe's Rayleigh conductivity [8] and $\bar{u}$ is the mean flow velocity within the hole. L denotes the acoustic effective length of the hole, equal to the hole length plus an end correction term, typically $8D/3\pi$ [30].

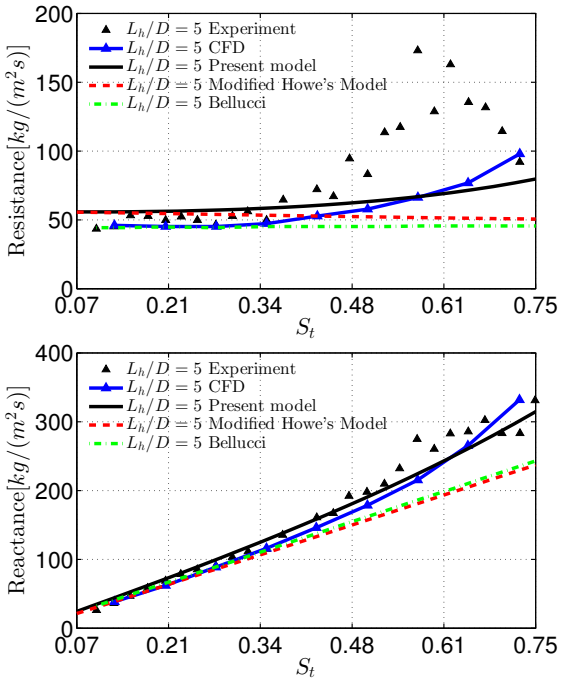

Figure 14: Validation of the real and imaginary parts of the hole impedance variation with Strouhal number for a hole of length to diameter ratio $L_h/D = 5$. The Reynolds number based on the hole diameter is approximately 13000. Experimental and CFD results from Su et al. [15], the Modified Howe's Model [8] applies a compact hole mass inertial correction from [10], Bellucci's semi-empirical model [3] uses the measured discharge coefficient from [15].

The variation of the impedance with Strouhal number for long holes with $L_h/D = 5$ and $L_h/D = 10$ are shown in Figs. 14 and 15 respectively. The experimental data shows that both the resistance and reactance exhibit nonlinear behaviour with increasing Strouhal number (especially at higher frequencies), and this is not well-captured by either the Modified Howe's Model or the semi-empirical Bellucci model. The present model predicts the same impedance as previous models at low frequencies, and is also able to predict the nonlinear variation of both the resistance and reactance at higher frequencies. The low frequency match between the present and previous models follows straightforwardly from Eq. (53) which reduces to the Modified Howe's Model when $(\omega\bar{c}L)/(\bar{c}^2 - \bar{u}^2)$ tends to zero (and reduces to Howe's model if $L = 0$). At higher frequencies, the reactance increases faster than the linear rate; both the CFD method and the present method capture this trend very well. For the resistance, these long holes show a very different behaviour from that of short holes – the resistance increases, rather than decreasing with Strouhal number (frequency). Note that the experimental measurement error for resistance increases with frequency, where the reactance starts to significantly exceed the resistance [15].

5. Conclusions

Previous analytical models based on Howe's model [8] have recently been shown insufficient for accurately capturing acoustic impedance of short but finite length circular holes. This article has presented a new analytical model based on the Green's function method for such holes. This model offers physical insights and time savings over fully computational methods.

For a "short" hole, not long enough to allow the separated mean flow from the front lip (hole inlet edge) to reattach within the hole, the importance of capturing the vortex-sound interaction accurately is shown. Both the hole length

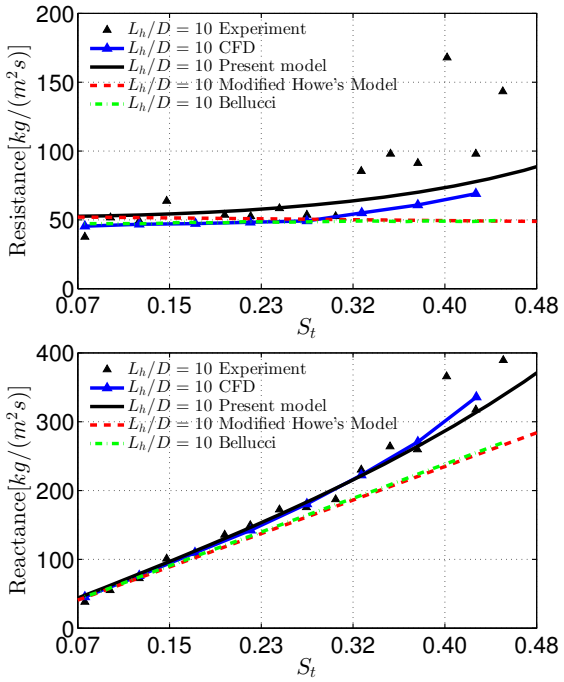

Figure 15: Validation of the real and imaginary parts of the hole impedance variation with Strouhal number for a hole of length to diameter ratio $L_h/D = 10$. The Reynolds number based on the hole diameter is approximately 12500. Experimental and CFD results from Su et al. [15], the Modified Howe's Model [8] applies a compact hole mass inertial correction from [10], Bellucci's semi-empirical model [3] uses the measured discharge coefficient from [15].

and the vortex sheet shape (the path of vortices) are shown to affect the predicted hole impedance greatly. More specifically, a hole whose length is between its radius and diameter shows the potential for vortex-sound coupling to generate rather than absorb acoustic energy at low Strouhal numbers. Accurately predicting the acoustic response of these holes requires accurate knowledge of the vortex sheet shape. Using a vortex sheet path provided by experimental data, the developed model achieves good agreement with the experimentally measured impedance. The effect of the vortex sheet path near the hole inlet edge and its fully contracted radius far-downstream has been studied, revealing that the importance of vortex sound interaction inside the hole increases when the near edge vortex path is less steep, or when the fully developed vortex sheet radius is larger.

For longer holes, in which the separated mean flow reattaches within the hole, a simplified model combining Howe's model for an infinitesimally short hole with non-compact modelling of the plane acoustic waves inside the hole predicts the hole acoustic impedance in good agreement with experiment measurements. The hole non-compactness leads to nonlinearly increasing resistance and reactance at higher frequencies.

The models developed in this paper can be implemented computationally in very little time, and are ideal for embedding in models of more complex systems such as aero-engine and gas turbine combustors.

Acknowledgements

Dong Yang is supported by a PhD scholarship from the Chinese Scholarship Council and Imperial College London which is gratefully acknowledged. The financial support of Dr. Aimee S. Morgans' ERC Starting Grant, ACOULOMODE (2013-18), is also acknowledged. Jialin Su, Dr. Andrew Garmory and Prof. Jon Carrotte from Loughborough University, and Dr. Jochen Rupp from Rolls-Royce are also gratefully acknowledged for kindly sharing their experimental and CFD data.

Appendices

A. Calculating the Green's functions for short finite length holes

In the frequency domain, Eq. (4) can be written as

$$\left(\frac{1}{\bar{c}^2}\left(-\mathrm{i}\omega+\bar{u}\frac{\partial}{\partial x_1}\right)^2-\nabla^2\right)\widetilde{G}=\delta(\boldsymbol{x}-\boldsymbol{y}). \tag{A.1}$$

In the upstream region, to satisfy $\partial\widetilde{G}_u/\partial r_x=0$ at $r_x=R_u$, $\widetilde{G}_u$ is expanded as a sum of a series of Bessel functions

$$\widetilde{G}_u=\sum_{n=0}^{+\infty}a_nJ_0(j_nr_x/R_u). \tag{A.2}$$

Using the general solutions to the homogeneous acoustic wave equation, $\widetilde{G}_u$ can be written as summations of upstream and downstream propagating waves on either side of the acoustic source $\boldsymbol{y}$.

$$\widetilde{G}_u=\sum_{n=0}^{+\infty}\left(A_{n1}e^{\mathrm{i}k_u^{n+}x_1}+A_{n2}e^{\mathrm{i}k_u^{n-}x_1}\right)J_0(j_nr_x/R_u),\quad -\infty<y_1\le x_1\le 0 \tag{A.3}$$

$$\widetilde{G}_u=\sum_{n=0}^{+\infty}\left(B_{n1}e^{\mathrm{i}k_u^{n+}x_1}+B_{n2}e^{\mathrm{i}k_u^{n-}x_1}\right)J_0(j_nr_x/R_u),\quad -\infty<x_1\le y_1\le 0 \tag{A.4}$$

where $k_u^{n+}=-k\bar{M}_u+\gamma_u^{(n)}$ and $k_u^{n-}=-k\bar{M}_u-\gamma_u^{(n)}$ are the downstream and upstream propagating wavenumber respectively (second-order terms $\sim\bar{M}_u^2$ are neglected). $\partial\widetilde{G}_u/\partial x_1=0$ on $x_1=0^-$ requires

$$\mathrm{i}k_u^{n+}A_{n1}+\mathrm{i}k_u^{n-}A_{n2}=0, \tag{A.5}$$

and only outward propagating waves at $x_1=-\infty$ requires

$$B_{n1}=0. \tag{A.6}$$

The following steps use a similar idea to those used in [31]. Equations (A.3) and (A.4) can be combined to give

$$\widetilde{G}_u(\boldsymbol{x},\boldsymbol{y},\omega)=H(x_1-y_1)\sum_{n=0}^{+\infty}\left(A_{n1}e^{\mathrm{i}k_u^{n+}x_1}+A_{n2}e^{\mathrm{i}k_u^{n-}x_1}\right)J_0(j_nr_x/R_u)+H(y_1-x_1)\sum_{n=0}^{+\infty}\left(B_{n1}e^{\mathrm{i}k_u^{n+}x_1}+B_{n2}e^{\mathrm{i}k_u^{n-}x_1}\right)J_0(j_nr_x/R_u), \tag{A.7}$$

where H is the Heaviside function. Substituting Eq. (A.7) into Eq. (A.1) and using the relations $\partial H(x_1-y_1)/\partial x_1=\delta(x_1-y_1)$ and $\partial\delta(x_1-y_1)/\partial x_1=\delta'(x_1-y_1)$, we finally get the relation

$$\begin{aligned}
&\sum_{n=0}^{+\infty}\delta(x_1-y_1)\Big[-2\mathrm{i}k\bar{M}_u\left(A_{n1}e^{\mathrm{i}k_u^{n+}x_1}+A_{n2}e^{\mathrm{i}k_u^{n-}x_1}-B_{n1}e^{\mathrm{i}k_u^{n+}x_1}-B_{n2}e^{\mathrm{i}k_u^{n-}x_1}\right)\\
&+(\bar{M}_u^2-1)\left(\mathrm{i}k_u^{n+}A_{n1}e^{\mathrm{i}k_u^{n+}x_1}+\mathrm{i}k_u^{n-}A_{n2}e^{\mathrm{i}k_u^{n-}x_1}-\mathrm{i}k_u^{n+}B_{n1}e^{\mathrm{i}k_u^{n+}x_1}-\mathrm{i}k_u^{n-}B_{n2}e^{\mathrm{i}k_u^{n-}x_1}\right)\Big]J_0(j_nr_x/R_u)\\
&-\sum_{n=0}^{+\infty}\delta'(x_1-y_1)\Big[A_{n1}e^{\mathrm{i}k_u^{n+}x_1}+A_{n2}e^{\mathrm{i}k_u^{n-}x_1}-B_{n1}e^{\mathrm{i}k_u^{n+}x_1}-B_{n2}e^{\mathrm{i}k_u^{n-}x_1}\Big]J_0(j_nr_x/R_u)\\
&=\delta(x_1-y_1)\delta(r_x-r_y)/(2\pi r_x).
\end{aligned}$$

Multiplying $2\pi J_0(j_nr_x/R_u)r_x$ and integrating from $r_x=0$ to $r_x=R_u$ on both sides, then matching the coefficients of $\delta(x_1-y_1)$ and $\delta'(x_1-y_1)$ on both sides gives

$$A_{n1}e^{\mathrm{i}k_u^{n+}y_1}+A_{n2}e^{\mathrm{i}k_u^{n-}y_1}-B_{n1}e^{\mathrm{i}k_u^{n+}y_1}-B_{n2}e^{\mathrm{i}k_u^{n-}y_1}=0, \tag{A.8}$$

$$\mathrm{i}k_u^{n-}A_{n1}e^{\mathrm{i}k_u^{n+}y_1}+\mathrm{i}k_u^{n+}A_{n2}e^{\mathrm{i}k_u^{n-}y_1}-\mathrm{i}k_u^{n-}B_{n1}e^{\mathrm{i}k_u^{n+}y_1}-\mathrm{i}k_u^{n+}B_{n2}e^{\mathrm{i}k_u^{n-}y_1}=\frac{J_0(j_nr_y/R_u)}{\pi R_u^2J_0^2(j_n)}. \tag{A.9}$$

Equations (A.5,A.6, A.8,A.9) are then combined to give

$$A_{n1} = \frac{\mathrm{i}J_0(j_n r_y/R_u)}{2\pi R_u^2 J_0^2(j_n)\gamma_u^{(n)}} e^{-\mathrm{i}k_u^{n+}y_1}, \tag{A.10}$$

$$A_{n2} = \frac{-\mathrm{i}J_0(j_n r_y/R_u)k_u^{n+}}{2\pi R_u^2 J_0^2(j_n)\gamma_u^{(n)}k_u^{n-}} e^{-\mathrm{i}k_u^{n+}y_1}, \tag{A.11}$$

$$B_{n1} = 0, \tag{A.12}$$

$$B_{n2} = \frac{\mathrm{i}J_0(j_n r_y/R_u)}{2\pi R_u^2 J_0^2(j_n)\gamma_u^{(n)}} \left(e^{-\mathrm{i}k_u^{n-}y_1} - \frac{k_u^{n+}}{k_u^{n-}} e^{-\mathrm{i}k_u^{n+}y_1} \right). \tag{A.13}$$

Thus, the upstream Green's function is finally written as

$$\widetilde{G}_u = \sum_{n=0}^{+\infty} \frac{\mathrm{i}J_0(j_n r_x/R_u)J_0(j_n r_y/R_u)}{2\pi R_u^2 \gamma_u^{(n)} J_0^2(j_n)} \left[e^{\mathrm{i}\gamma_u^{(n)}|x_1-y_1|} - \frac{k_u^{n+}}{k_u^{n-}} e^{-\mathrm{i}\gamma_u^{(n)}(x_1+y_1)} \right] e^{\mathrm{i}k\bar{M}_u(y_1-x_1)}. \tag{A.14}$$

The derivation process is similar for the other Green's functions.

References

[1] I. J. Hughes and A. P. Dowling. "The absorption of sound by perforated linings". In: *Journal of Fluid Mechanics* 218 (1990), pp. 299–335.

[2] J. D. Eldredge and A. P. Dowling. "The absorption of axial acoustic waves by a perforated liner with bias flow". In: *Journal of Fluid Mechanics* 485 (2003), pp. 307–335.

[3] V. Bellucci, P. Flohr, C. O. Paschereit, and F. Magni. "On the use of Helmholtz resonators for damping acoustic pulsations in industrial gas turbines". In: *Journal of Engineering for Gas Turbines and Power* 126.2 (2004), pp. 271–275.

[4] D. Zhao and X. Y. Li. "A review of acoustic dampers applied to combustion chambers in aerospace industry". In: *Progress in Aerospace Sciences* 74 (2015), pp. 114–130.

[5] P. Palies, T. Schuller, D. Durox, L. Y. M. Gicquel, and S. Candel. "Acoustically perturbed turbulent premixed swirling flames". In: *Physics of Fluids (1994-present)* 23.3 (2011), p. 037101.

[6] S. Candel, D. Durox, T. Schuller, J. F. Bourgouin, and J. P. Moeck. "Dynamics of swirling flames". In: *Annual Review of Fluid Mechanics* 46 (2014), pp. 147–173.

[7] M. S. Howe. "Attenuation of sound in a low Mach number nozzle flow". In: *Journal of Fluid Mechanics* 91.02 (1979), pp. 209–229.

[8] M. S. Howe. "On the theory of unsteady high Reynolds number flow through a circular aperture". In: *Proceedings of the Royal Society of London. A. Mathematical and Physical Sciences* 366.1725 (1979), pp. 205–223.

[9] J. C. Wendoloski. "Sound absorption by an orifice plate in a flow duct". In: *The Journal of the Acoustical Society of America* 104.1 (1998), pp. 122–132.

[10] X. Jing and X. Sun. "Experimental investigations of perforated liners with bias flow". In: *The Journal of the Acoustical Society of America* 106.5 (1999), pp. 2436–2441.

[11] I. D. J. Dupère and A. P. Dowling. "The use of Helmholtz resonators in a practical combustor". In: *Journal of Engineering for Gas Turbines and Power* 127.2 (2005), pp. 268–275.

[12] J. Rupp, J. F. Carrotte, and A. Spencer. "Interaction between the acoustic pressure fluctuations and the unsteady flow field through circular holes". In: *Journal of Engineering for Gas Turbines and Power* 132.6 (2010), p. 061501.

[13] A. Scarpato, N. Tran, S. Ducruix, and T. Schuller. “Modeling the damping properties of perforated screens traversed by a bias flow and backed by a cavity at low Strouhal number”. In: *Journal of Sound and Vibration* 331.2 (2012), pp. 276–290.

[14] X. Jing and X. Sun. “Effect of plate thickness on impedance of perforated plates with bias flow”. In: *AIAA Journal* 38.9 (2000), pp. 1573–1578.

[15] J. Su, J. Rupp, A. Garmory, and J. F. Carrotte. “Measurements and computational fluid dynamics predictions of the acoustic impedance of orifices”. In: *Journal of Sound and Vibration* 352 (2015), pp. 174–191.

[16] H. Rouse and A. Abul-Fetouh. “Characteristics of irrotational flow through axially symmetric orifices”. In: *Journal of Applied Mechanics-Transactions of the ASME* 17.4 (1950), pp. 421–426.

[17] D. Rockwell and E. Naudascher. “Self-sustained oscillations of impinging free shear layers”. In: *Annual Review of Fluid Mechanics* 11.1 (1979), pp. 67–94.

[18] M. S. Howe. *Hydrodynamics and Sound*. Cambridge University Press, 2006.

[19] P. Testud, Y. Aurégan, P. Moussou, and A. Hirschberg. “The whistling potentiality of an orifice in a confined flow using an energetic criterion”. In: *Journal of Sound and Vibration* 325.4 (2009), pp. 769–780.

[20] A. Kierkegaard, S. Allam, G. Efraimsson, and M. Åbom. “Simulations of whistling and the whistling potentiality of an in-duct orifice with linear aeroacoustics”. In: *Journal of Sound and Vibration* 331.5 (2012), pp. 1084–1096.

[21] J. Li and A. S. Morgans. “Time domain simulations of nonlinear thermoacoustic behaviour in a simple combustor using a wave-based approach”. In: *Journal of Sound and Vibration* 346 (2015), pp. 345–360.

[22] M. S. Howe. *Acoustics of Fluid-Structure Interactions*. Cambridge University Press, 1998.

[23] I. D. J. Dupère and A. P. Dowling. “The absorption of sound near abrupt axisymmetric area expansions”. In: *Journal of Sound and Vibration* 239.4 (2001), pp. 709–730.

[24] M. S. Howe. *Theory of Vortex Sound*. Vol. 33. Cambridge University Press, 2003.

[25] G. N. Watson. *A Treatise on the Theory of Bessel Functions*. Cambridge University Press, 1995.

[26] S. Mendez and J. D. Eldredge. “Acoustic modeling of perforated plates with bias flow for large-eddy simulations”. In: *Journal of Computational Physics* 228.13 (2009), pp. 4757–4772.

[27] B. S. Massey and J. Ward-Smith. *Mechanics of Fluids*. Vol. 1. CRC Press, 1998.

[28] F. Durst, W. F. Schierholz, and A. M. Wunderlich. “Experimental and numerical investigations of plane duct flows with sudden contraction”. In: *Journal of Fluids Engineering* 109.4 (1987), pp. 376–383.

[29] P. R. Bullen, D. J. Cheeseman, and L. A. Hussain. “The effects of inlet sharpness on the pipe contraction pressure loss coefficient”. In: *International Journal of Heat and Fluid Flow* 9.4 (1988), pp. 431–433.

[30] L. E. Kinsler, A. R. Frey, A. B. Coppens, and J. V. Sanders. *Fundamentals of Acoustics*. 4th Edition. Vol. 1. Wiley-VCH, December 1999.

[31] M. A. Heckl and M. S. Howe. “Stability analysis of the Rijke tube with a Green’s function approach”. In: *Journal of Sound and Vibration* 305.4 (2007), pp. 672–688.